TECHNICAL ARTICLE

Corrosion of 1.4016 Ferritic Steel by Urea at High Temperature

Anastasiia Galakhova, Fabian Kadisch, Gregor Mori, Susanne Heyder, Helmut Wieser, Bernhard Sartory, Jaroslaw Wosik, Sabine Schwarz, and Simon Burger

The corrosion behavior of a ferritic unstabilized stainless steel 1.4016 during decomposition of aqueous urea solution at high temperature has been investigated. Corrosion was obtained from 100 h of cyclic heating (from room temperature up to 600 °C) and injection of aqueous urea solution on the steel plate in a laboratory-scale test bench. The evaluation procedure covered the metallographic analysis of corroded steel samples by high-resolution scanning electron microscopy (HR-SEM) and transmission electron microscopy (TEM). Uniform corrosion underneath deposits was found as one of the drivers for degradation of the steel. Damage happened by high-temperature depassivation of stainless steel due to the excess of the aggressive medium. Besides uniform corrosion, a nitridation layer underneath surface oxides together with chromium carbonitride particles precipitated through the whole depth of the sample was identified resulting in intergranular attack.

1. Introduction

Ferritic stainless steels are known to have good corrosion and high-temperature oxidation resistances, as preferentially oxidized chromium results in formation of a Cr-rich oxide layer, which is responsible for the retarding of the oxidation reaction (Ref 1-3). Ferritic steels also possess a low thermal expansion coefficient, what is beneficial for hot applications (Ref 4, 5). Such type of steels can be stabilized and not stabilized depending on the application demands, and the difference between them is the addition of Nb, V, Ti and other alloying elements. For example, Nb is used to achieve a thermal fatigue resistance, as it helps to form a Laves phase between the oxide layer and the matrix preventing the diffusion of cations to the oxide layer and inhibiting the oxygen to get into the steel (Ref 2, 3). 1.4016 is a low carbon, 16% chromium, not stabilized stainless steel, which has a good corrosion and oxidation resistance, formability, ductility and mechanical properties (Ref 6).

Corrosion of stainless steels at high temperature in urea is rarely investigated. This type of corrosion may occur in urea or cyanuric acid production, fertilizer industry or selective catalytic reduction (SCR) technology (Ref 7, 8), where the steel is corroded not only by aggressive chemical environment, but also by high thermal fatigue. Several mechanisms for urea corrosion are described in the literature. Among them are cyclic oxidation caused by thermal cycling (Ref 7), external corrosion by road salts (Ref 9, 10), nitriding and carburization reagents. There melamine, cyanuric acid, ammonia, nitrogen or graphite-like phase of C_3N_4 (g-C_3N_4) chemically react with metal oxides to form nitride or carbide particles (Ref 11-13). Most frequently the degradation of steel is described by fracture and attacks along grain boundaries attributed to chromium depletion and carbonitride precipitates (Ref 7, 8, 13-16). However, precipitates at grain boundaries have been found not only rarely (Ref 4, 5, 8).

Recently, we have investigated a complex mechanism of high-temperature urea corrosion of ferritic steel 1.4509 (Ref 17). For this purpose, we have analyzed all products of urea decomposition reactions at high temperature and correlate them with temperature and pH value, at which they could lead to corrosion of the steel. As a result of 100 h of cyclic heating and injection of aqueous urea solution on steel sample, the material showed large uniform corrosion underneath of deposits and attacks along grain boundaries. However, neither precipitation nor chromium depletion along grain boundary was found.

In the current study, we continue to investigate the corrosion phenomenon of ferritic stainless steel by hot urea solution. It includes the metallographic analysis of the corroded steel sample by SEM (scanning electron microscope), HR-SEM (high-resolution SEM) and TEM (transmission electron micro-

---

Anastasiia Galakhova, Fabian Kadisch, and **Gregor Mori**, Chair of General and Analytical Chemistry, Montanuniversität Leoben, Franz Josef-Strasse 18, 8700 Leoben, Austria; **Susanne Heyder** and **Helmut Wieser**, Faculty of Mechanical and Process Engineering, Augsburg University of Applied Sciences, An Der Hochschule 1, 86161 Augsburg, Germany; **Bernhard Sartory** and **Jaroslaw Wosik**, Materials Center Leoben Forschung GmbH, Roseggerstrasse 12, 8700 Leoben, Austria; **Sabine Schwarz**, University Service Centre for Transmission Electron Microscopy USTEM, Technische Universität Wien, Wiedner Hauptstraße 8-10, 1040 Vienna, Austria; and **Simon Burger**, Faurecia Emissions Control Technologies, Germany GmbH, 86154 Augsburg, Germany. Contact e-mails: Anastasia.Galakhova@gmail.com, Fabian.Kadisch@unileoben.ac.at, Mori@unileoben.ac.at, Susanne.Heyder@hs-augsburg.de, Helmut.Wieser@hs-augsburg.de, Bernhard.Sartory@mcl.at, Yaroslaw.Wosik@mcl.at, Sabine.Schwarz@tuwien.ac.at, and simon.burger@faurecia.com.

scope). The presence of precipitates on grain boundaries is investigated to verify the origin of intergranular corrosion by nitridation or/and carburization.

2. Materials and Methods

2.1 Materials

As sample material, stainless ferritic non-stabilized grade 1.4016 has been selected. The material has a purely ferritic microstructure with a fine grain size between 10 and 30 μm. The chemical composition of the steel is 0.055% C, 0.28% Si, 0.513% Mn, 16.44% Cr, 0.03% P and 0.004% S. An aqueous urea solution for the corrosion experiment consisted of 32.5% urea and 67.5% deionized water.

2.2 Corrosion Experiment

The corrosion experiment was performed in the closed chamber where the steel specimen is exposed to 100 h of cyclic heating (from room temperature up to 600 °C) and injection of aqueous urea solution, and the photograph and schematic illustration are shown in Fig. 1(a) and (b). The temperature cycle and other parameters of the corrosion experiment are described in detail in a previous work (Ref 17).

2.3 Characterization Methods

The analysis of the corroded specimen cross section was done using field-emission gun scanning electron microscopy (FE-SEM/GeminiSEM 450, Carl Zeiss SMT, Oberkochen, Germany) coupled with window less energy-dispersive X-ray detector (EDX/Ultim Extreme, Oxford Instruments NanoAnalysis, Bucks, UK). The energy-dispersive spectroscopic (EDS) point analysis was done with the interaction volume of 0.3 μm. As soon as the 100 h corrosion experiment was completed (Fig. 2a), the specimen in the chamber was cleaned from deposits (Fig. 2b) and two parts of the steel specimen were disconnected (Fig. 2c). The FE-SEM analysis was done on a polished cross section, which was cut out of baseplate. The location of cutting of the cross section is shown by the dashed

line and direction of examination by arrows A and B in Fig. 2(c). The structure of the precipitates was examined by transmission electron microscopy (TEM/FEI Tecnai F20, FEG, 200 kV operation voltage, USA) coupled with EDX (EDAX Apollo XLTW SSD detector, AMETEK Inc., USA), and the corresponding sample was prepared by help of focused ion beam instrument (FIB/Thermo Fisher Scientific Scios 2 DualBeam, USA). Prior to energy-dispersive X-ray measurement, the system has been calibrated with a 316 stainless steel standard containing 17.2% Cr, 11.3% Ni and 2.1% Mo. It can be seen in the results that all quantitative EDS analyses of the investigated steel matrix give reliable concentrations of alloying elements.

3. Results

After 100 h of cyclic heating and injection of aqueous urea solution on the steel 1.4016, the material shows a differently colored, oxidized surface (Fig. 2a, b and c). The material loss is localized near the crevice where two steel design parts were in contact (Fig. 2c). There are also areas along the boundary (where two steel design parts were in contact, marked by green dotted line) with no material loss found, probably due to a more narrow crevice between them (Fig. 2c).

3.1 Metallographic Analysis of Corroded Area A

3.1.1 SEM Analysis. Examining the cross section of the corroded area A (microscopic image in Fig. 3(a), for macroscopic image look at yellow dashed line in Fig. 2c), one can observe parts that are slightly corroded and parts that are more attacked. The total wall thickness of the investigated steel sheet was 1.6 mm before testing and in the slightly corroded area after the experiment no reduction of wall thickness was detected with a caliper (caliper accuracy $\pm$ 10 μm). In the center of the SEM image (Fig. 3a) can be seen the strongly attacked area, with an indication of attack along grain boundaries as well as uniformly. Here, the material loss is 650 $\pm$ 50 μm and most of the grains tend to fall off. To the left
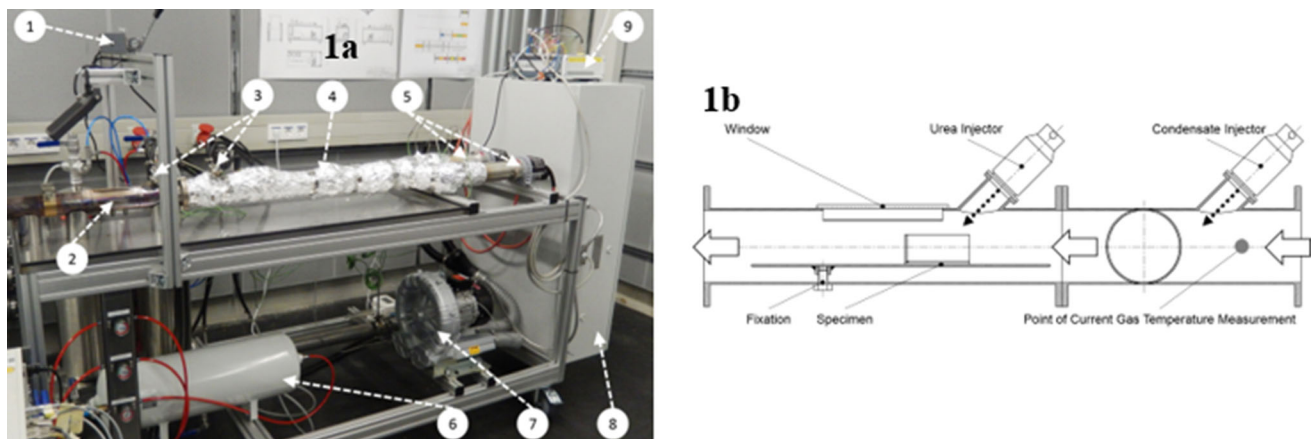

Fig. 1 (a) Photograph of test bench and (b) schematic illustration of the test track in the laboratory of University of Applied Sciences in Augsburg. Elements in test bench photograph: 1—camera mount, 2—test track, 3—injectors, 4—insulated test track part, 5—heating elements, 6—compressed air storage, 7—strong blower, 8—electric control cabinet, 9—real-time interface. Figure a and b is reproduced with permission from Arndt Tassilo 2019
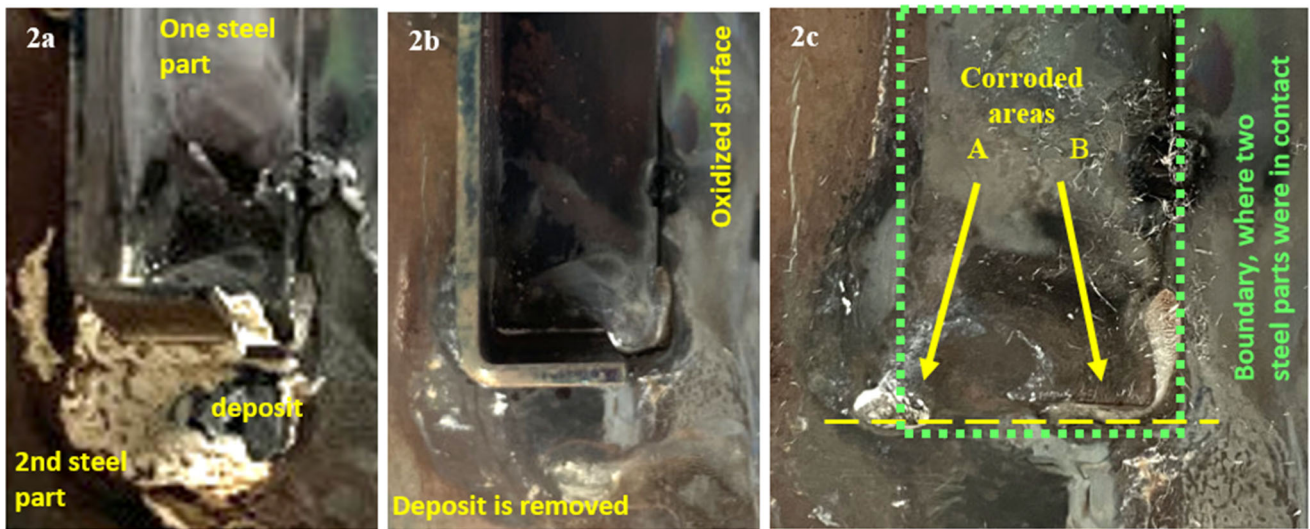
Fig. 2 Macroscopic image of corroded sample after 100 h experiment, 1.4016 grade. (a) Two steel design parts are in contact, not cleaned from urea-related deposits, (b) two steel design parts are in contact, cleaned from urea-related deposits, and (c) one separated steel design part with corroded areas shown by yellow arrows A and B along the yellow dashed line. Both corroded areas were subjected to metallographic analysis (Color figure online)
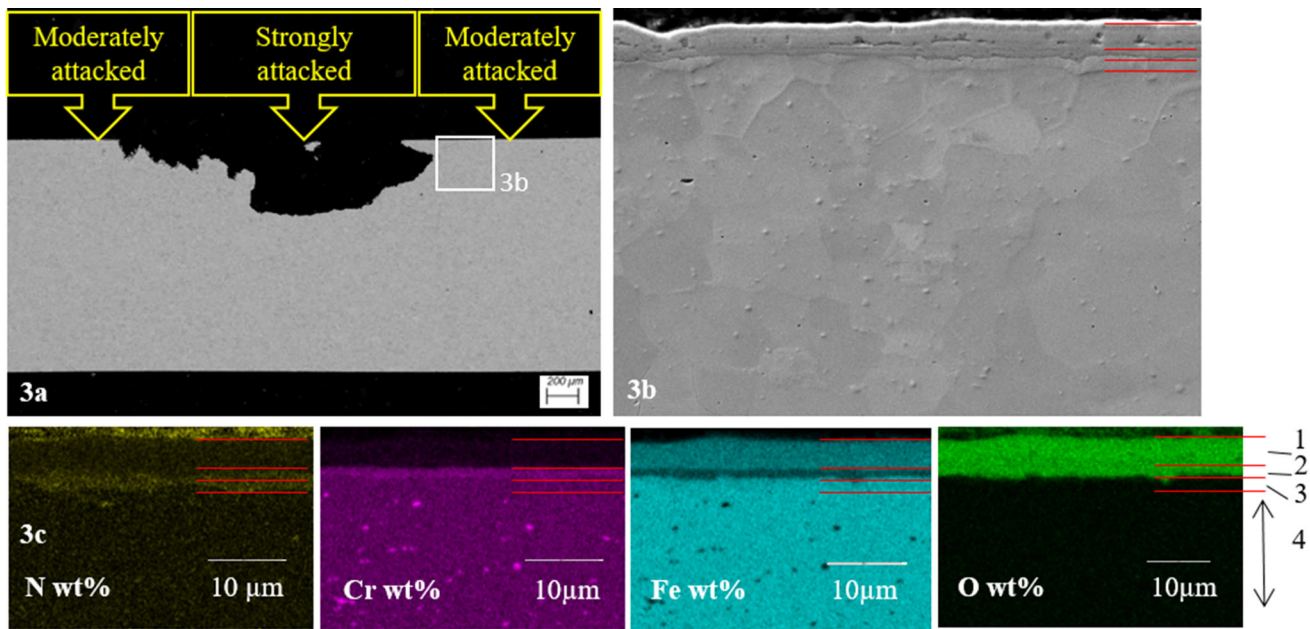

Fig. 3 FE-SEM image of the corroded sample in area A after 100 h experiment. (3a) BS detector, (3b) SE detector, (3c) EDS image by element distribution mapping shows three layers: 1—FeO$_x$ with a bit of Cr$_2$O$_3$; 2—Cr$_2$O$_3$; 3—nitrogen and 4—matrix

and right from the strongly attacked area, a moderately attacked region is visible when looking under higher magnification. (The place of interest is highlighted by white frame in Fig. 3a, and magnified in Fig. 3b.) This region of interest indicates multilayers on the surface (Fig. 3b). The element mapping of multilayers between surface and matrix is shown in Fig. 3c. Additionally, the concentration profile of the involved elements of the same location is shown in Fig. 4. The EDS analysis revealed the presence of 3 different layers. Starting from the outside, the depth profile shows FeO$_x$ with a bit of Cr$_2$O$_3$ at the surface (layer 1), under which a chromium-rich oxide (Cr$_2$O$_3$) layer can be seen (layer 2). The inner chromium oxide layer also appears to contain some FeO. At the oxide/metal interface, a high level of nitrogen was found (layer 3). When looking at the whole width of the sample, it is noticeable that the nitrogen layer is not constant and sometimes drops. In small quantities, nitrogen was found in the oxide layers. The results of chemical analysis by element mapping are in full agreement with the concentration profiles of the involved elements. Neither a sign of nitrogen nor any precipitation of chromium-rich phases at
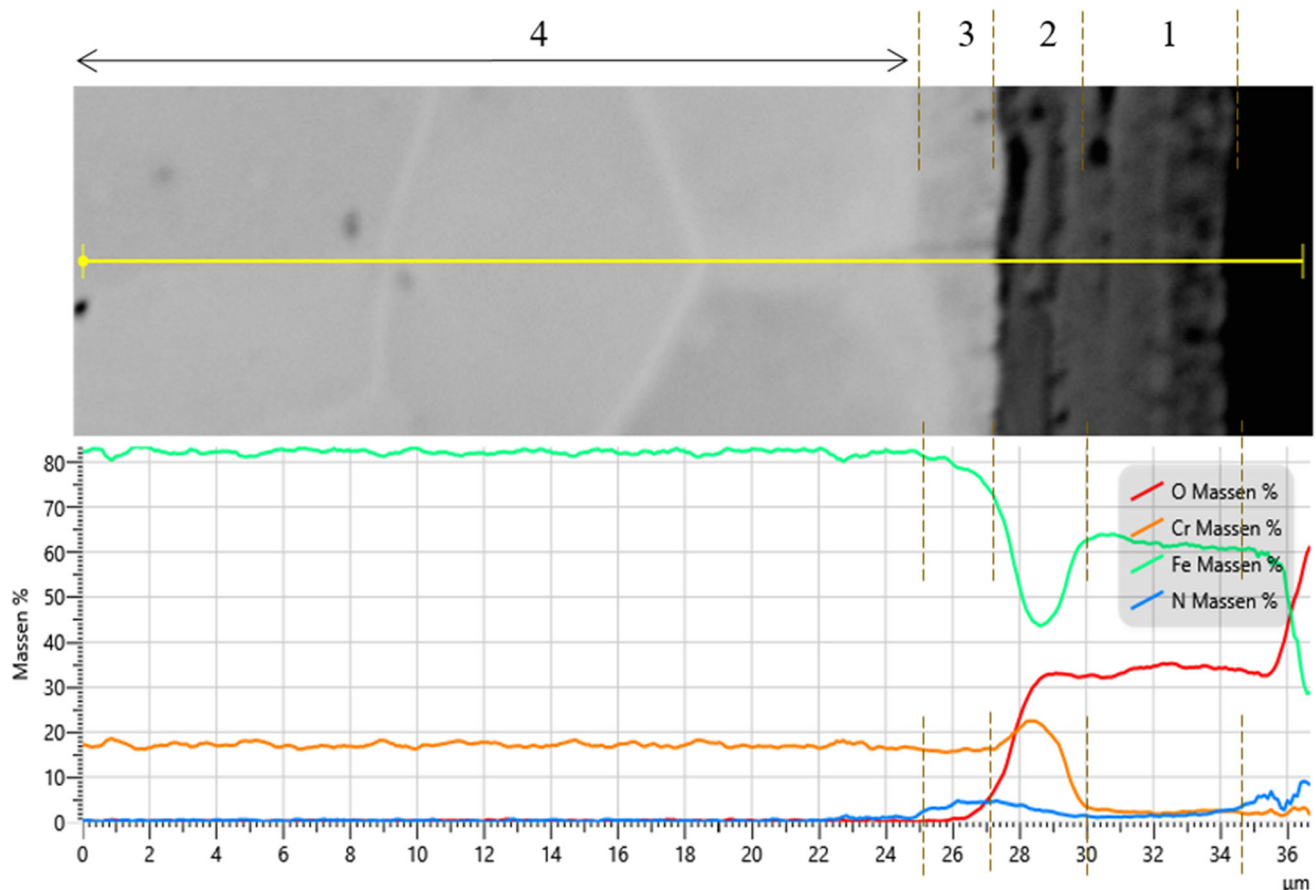
Fig. 4 Element concentration profile of the corroded sample in area A after 100 h experiment shows three layers: 1—FeO_x with a bit of Cr_2O_3, 2—Cr_2O_3, 3—nitrogen, and 4—matrix

the grain boundaries was observed by SEM–EDS. The total thickness of three O- and N-rich layers is 10 μm. The outer FeO-rich layer has a thickness of 5 μm, and the inner Cr_2O_3 and the N-rich layer has a thickness between 2 and 3 μm each.

By help of SEM–EDS technique severe material loss, grain boundary attack and nitriding were identified. However, no any particles at the grain boundaries (as a prerequisite of intergranular corrosion) were detected, what could be a sign of low resolution of SEM–EDS technique. Thus, investigation on the same corroded area A was continued with high-resolution HR-SEM technique. In the place of material loss (Fig. 5a and b is a higher magnification of region of interest highlighted by white frame in Fig. 5a), it is visible that starting from the surface the grains are surrounded by corrosion products and till a certain depth level, all grains are attacked (Fig. 5c). HR-SEM analysis revealed circle-shaped precipitates with roughly 40 nm size visible by BS detector as black spots (Fig. 5d and e). SE detector showed that there are no holes (Fig. 5f). These precipitates were identified by EDS technique as 3% N, 18% Cr and 18% C what could say for $Cr_2N/CrCN$. The precipitates along the grain boundaries were found at all depth levels of the sample (up to 1500 μm depth). For comparison reasons, the analysis of the matrix revealed neither nitrogen nor a depletion of chromium. A more detailed TEM analysis on the nature of precipitates was done.

3.1.2 TEM Analysis. Based on the HR-SEM results, a more detailed analysis on the nature of precipitates was performed by transmission electron microscopy (TEM). For

this purpose, focused ion beam (FIB) instrument has been used to prepare a thin specimen from the same corroded area A (Fig. 6).

FIB lift-out specimen was prepared in a cross section geometry to produce a lamella perpendicular to the polished surface of the bulk sample. After selecting the region of interest for specimen extraction, Pt layers were deposited in order to protect and frame the region of interest (Fig. 6a). Afterward, "C"-shaped channels were milled around the Pt protected area (Fig. 6b). A "bridge" was left at one of the short edges of the specimen to support the specimen until it is cut free from the bulk sample. Finally, the specimen was lifted out of bulk sample by a micromanipulator needle and transferred to the FIB TEM grid holder at 90° angle between the surfaces of the specimen and the grid (Fig. 6c and d). The final FIB thinning of lamella was performed in two thicknesses: Thinner part is generally preferable for TEM analysis, and thicker part is preferable for EDS analysis (Fig. 6e and f).

STEM HAADF analysis revealed precipitates on the grain boundary, some of them have a symmetric spherical shape with 20 nm diameter, and another one shows an oval shape with 170 nm length (Fig. 7b and c). By Z-contrast, it is visible that the heavy elements (Fe 26) are more light-colored, and the lighter elements (Cr 24, Mn 25) are darker-colored. According to EDS analysis, these precipitates are rich in Cr and slightly in N when comparing with matrix (Fig. 7d). The results of chemical analysis by element mapping are in full agreement with the qualitative concentration profile of the involved elements (Fig. 8a and b). Although nitrogen and, for instance,
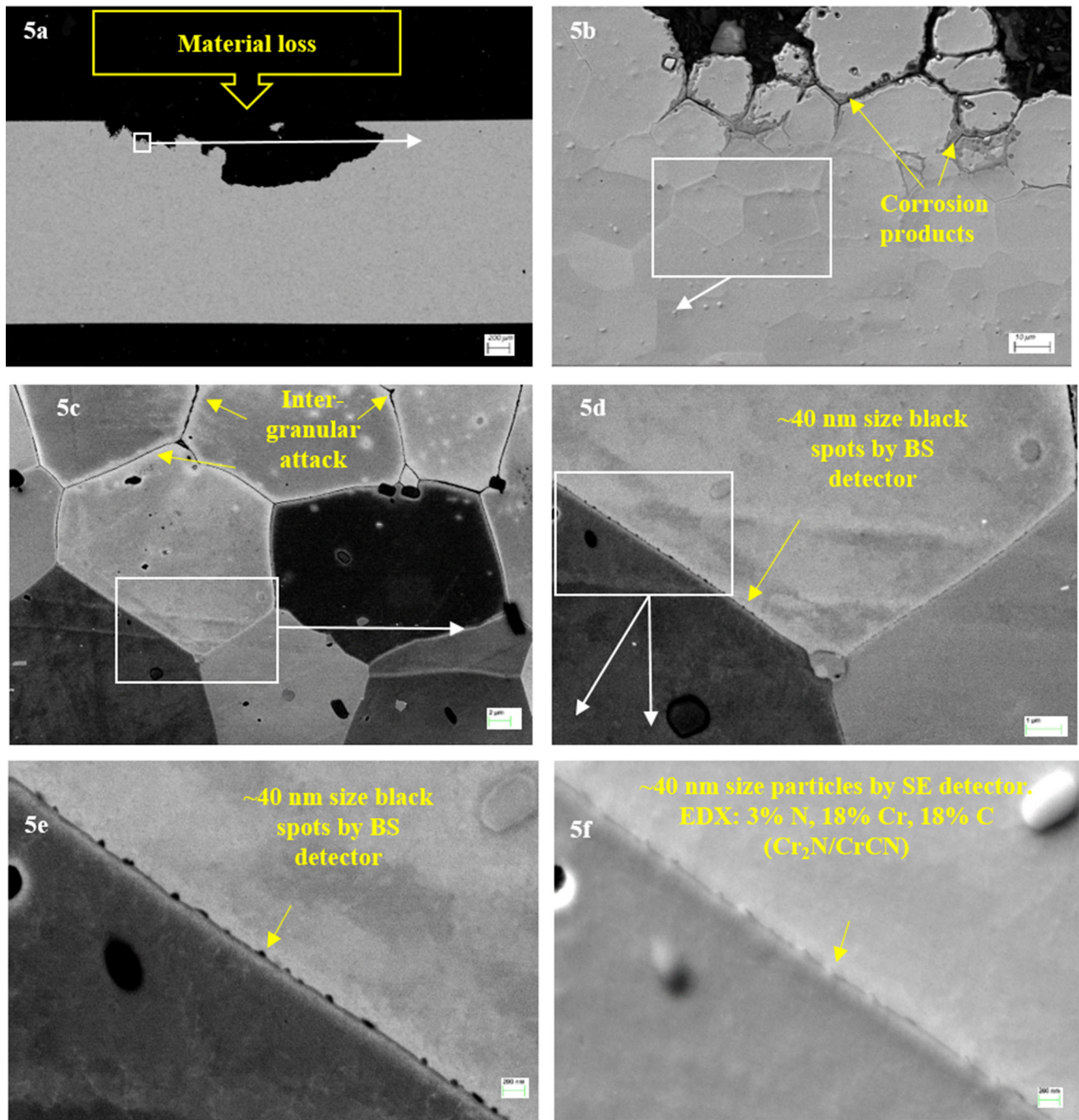
Fig. 5 FE-SEM image of the corroded sample in area A after 100 h experiment with a focus on corrosion products and precipitates on grain boundaries (**a, c, d, e** (BS detector) and **b, f** (SE detector): different magnifications)

carbon were more difficult to detect by EDS analysis with the described EDAX detector (see chapter 2.3), the analysis was possible even quantitatively, and the results of calculation clearly showed the presence of these two elements in the particle (Fig. 8c) when comparing with matrix (Fig. 8d). Even when quantitative EDS analysis of light elements such as carbon and oxygen is not reliable, the analysis of Fig. 8c and d shows substantial differences in carbon content on the same specimen. This is a strong argument that the precipitate in Fig. 8a contains carbon. The absolute value given in Fig. 8c is not too important.

Electron diffraction was performed on a TEM specimen of the same corroded area A. The obtained diffraction patterns from crystal orientations revealed the ferrite matrix and Cr_2N precipitates on the grain boundary (Fig. 9). When considering the high carbon content of the precipitates in Fig. 8c, the precipitates are not pure nitrides, but carbonitrides with the structure CrCN. The selected area for diffraction pattern of the dark-field TEM image is shown in Fig. 9a (red circle), the diffraction pattern in Fig. 9b and the calculated pattern of crystalline Cr_2N in zone axis [1, -1, 0] in Fig. 9c, which is in good agreement to the masked spots in Fig. 9b.
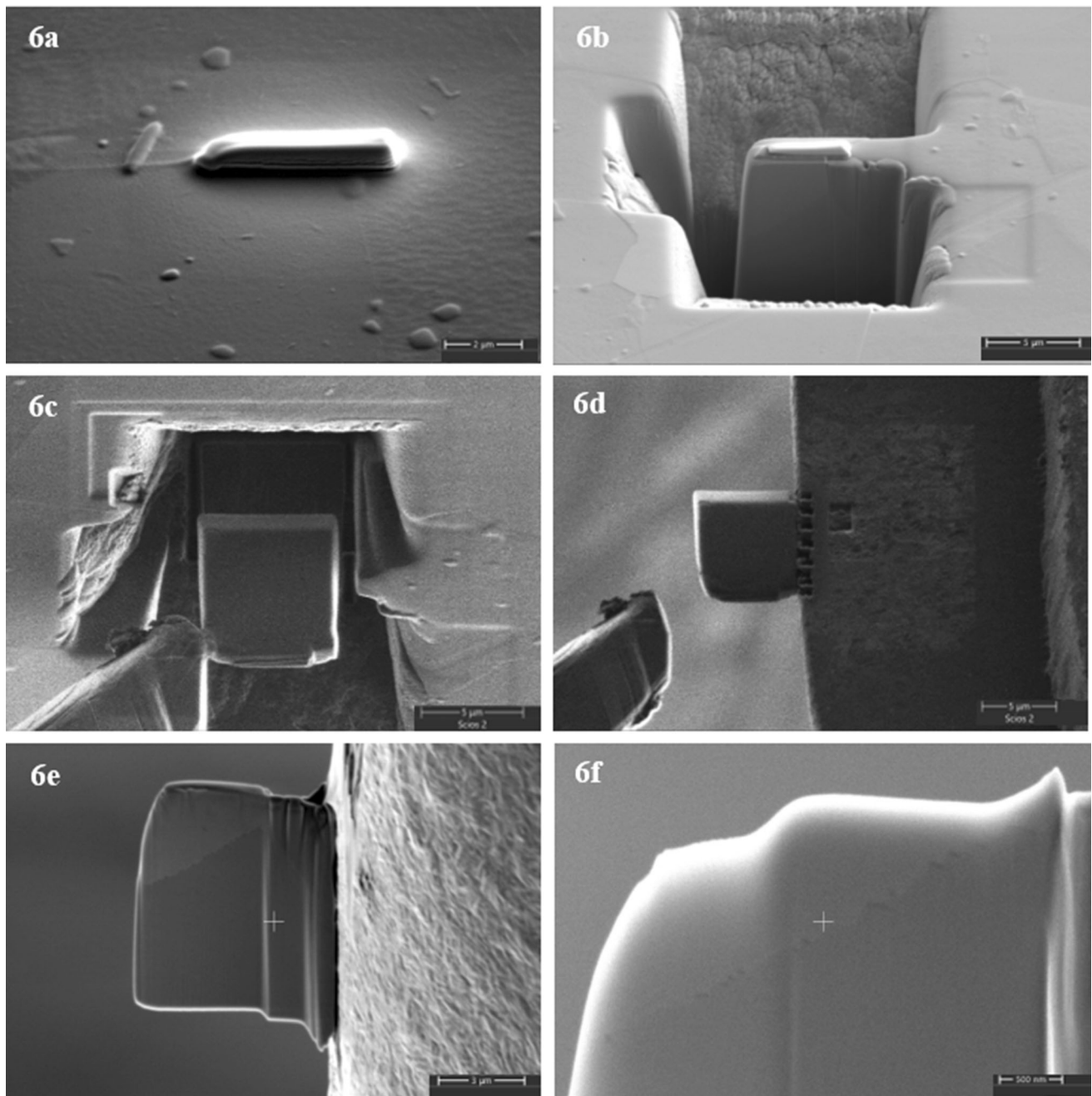
Fig. 6 FIB preparation of the lamella from the corroded sample in area A for TEM analysis. (a) Pt layer deposition, (b) "C" channel milling, (c, d) transfer of specimen to grid holder, (e, f) final thinning of lamella

3.2 Metallographic Analysis of Corroded Area B

Next to the corroded area A is located another characteristically corroded area B (Fig. 2c—macroscopic image, Fig. 10a—microscopic image). The cross section morphology of corroded area B exhibits also a moderately attacked region together with the strongly attacked one. In Fig. 10a, three regions of interest were selected for observation under higher magnification. (They are marked by the white frame, and each white arrow points out at a corresponding magnified image.) In Fig. 10f, the moderately attacked area displays the surface multilayer. Figure 10d and e shows the section, close to the severe material loss, with partial scaling of the surface multilayer,

where the grains are surrounded by corrosion products and are subjected to intergranular attack. In the deeper attacked area in Fig. 10b and c, one can easily see grains dropping.

4. Discussion

In this research work, a metallographic analysis of corrosive attack obtained after cyclic heating and injection of aqueous urea solution on the steel plate was performed. The sample was subjected to 100 cycles (1 cycle lasted one hour) in total. In our previous research work (Ref 17), the same experiment was
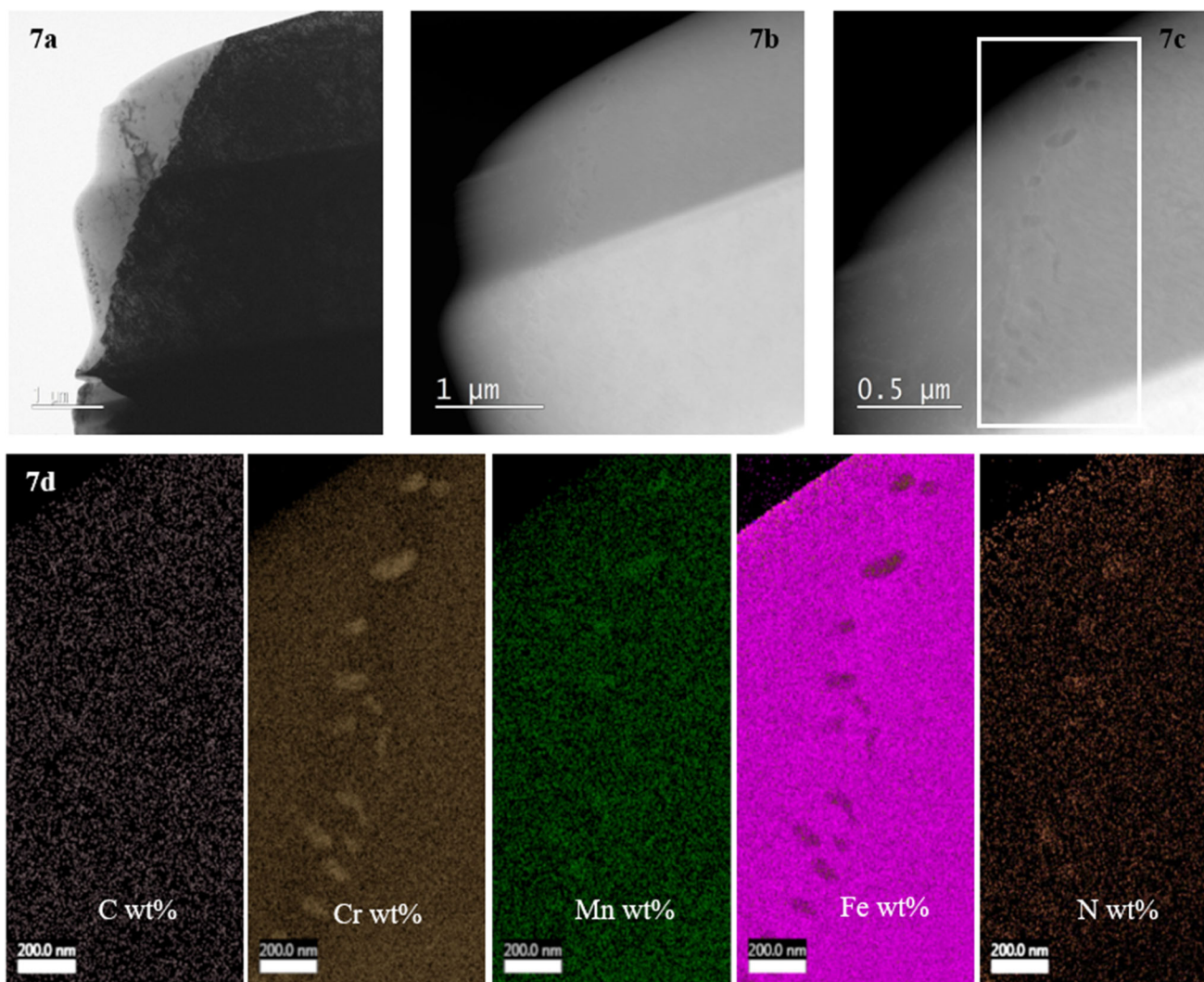
Fig. 7 STEM image of the grain boundary with precipitates and EDX image by element distribution mapping (corroded sample in area A after 100 h experiment, 1.4016 grade). (a) Lamella in TEM, (b) STEM HAADF image, (c, d) EDS map

performed with a different material grade. In that work (Ref 17), the material grade 1.4509 was studied together with obtained deposits consisting mainly of cyanuric acid and ammelide products. In addition to partially and completely exposed grains identified in the previous work, the corrosive attack in the current study exhibits a much higher material loss, clear visible attack along grain boundaries and chromium carbonitride precipitates. The weaker corrosion resistance of grade 1.4016, in comparison with grade 1.4509, could be explained by the chemical composition of the material. Material grade 1.4509 contains Nb, Ti and in a very small amount Mo, while molybdenum is known to increase the resistance of the material to acid dissolution, and that it forms a part of the oxide protective surface layer, stabilization elements Ti and Nb may catch the diffusing nitrogen and form NbN and TiN before chromium nitride is formed. The material grade 1.4016 does not contain any of the stabilization elements and in addition has a higher content of carbon and thus corrodes more severely. It also forms carbonitride grain boundary precipitates.

Already known from the previous study (Ref 17), the metal sample tends to corrode locally where urea-related products are likely to accumulate. During the long-term cyclic heating, the aqueous urea solution undergoes several chemical decomposition reactions which are responsible for the dissolution of the passive layer and the base metal. The dissolved cyanuric acid deposit (pH = 3.8) and/or gaseous isocyanic acid (pH = 3.7) may continuously decrease the pH value in the area of deposit accumulation, while the liquid phase of biuret and high humidity may support electrolyte formation necessary for uniform corrosion. Thus, wet acidic condition plays the major role in the corrosion mechanism of the described experiment.

Besides uniform corrosion, a nitriding phenomenon along grain boundaries was observed. Considering that urea decomposition products are rich in nitrogen, the diffusing nitrogen, generated nanoparticles and chromium depletion close to grain boundaries under high test temperature appears to be the second detrimental contribution to the corrosion mechanism. Precipitates that are rich in chromium (e.g., $Cr_2N/CrCN$) can be generated in ferritic stainless steels at substantially lower temperatures when compared to austenitic stainless steels. While in the austenite the highest rate of precipitation happens at approximately 800 °C, this temperature is 200 °C lower for the ferrite (at 600 °C) (Ref 18). Also, precipitation time in the ferrite is three orders of magnitude lower when compared to the
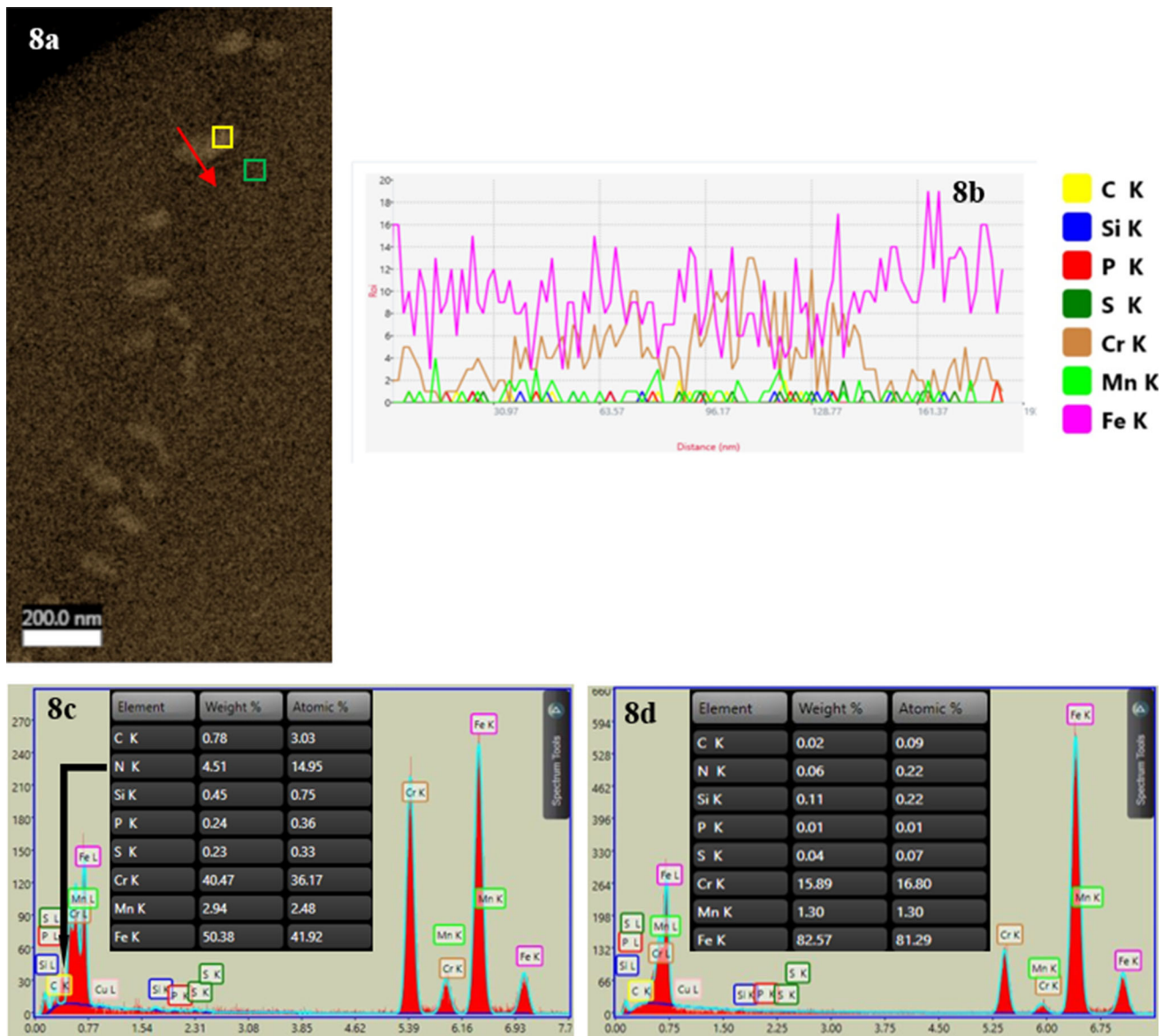
Fig. 8 (a) EDS image of the grain boundary with precipitates, (b) qualitative element concentration profile of one of the particles (marked by red arrow in 8a), (c) EDS measurement and quantification of elements in the area of particle (marked by yellow square in 8a), (d) EDS measurement and quantification of elements in the matrix (marked by green square in 8a)
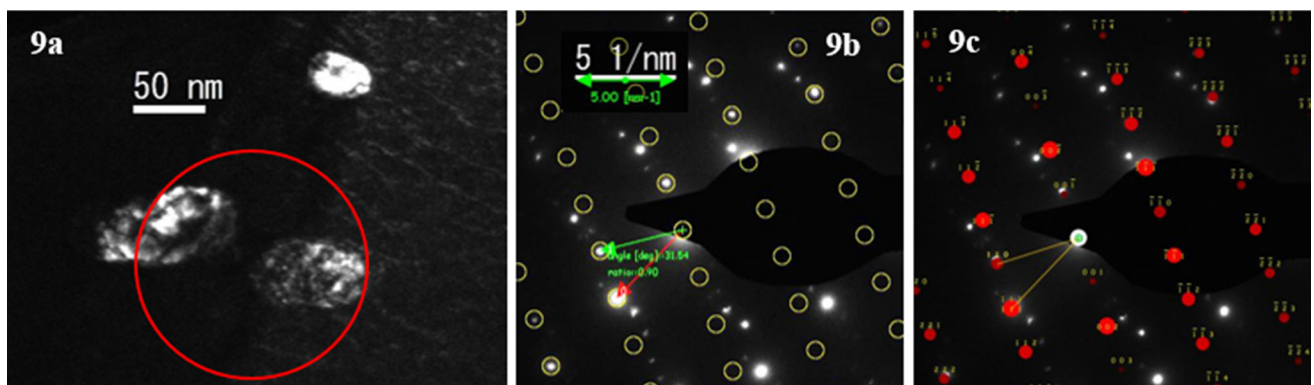

Fig. 9 TEM dark-field image and electron diffraction of grain boundary precipitates in material 1.4016. (a) TEM dark-field image of chromium-rich precipitates with selected area aperture (red circle), (b) corresponding diffraction pattern of selected area from figure b, (c) calculated diffraction pattern of Cr_2N in zone axis [1, −1, 0] compared to diffraction pattern in figure b
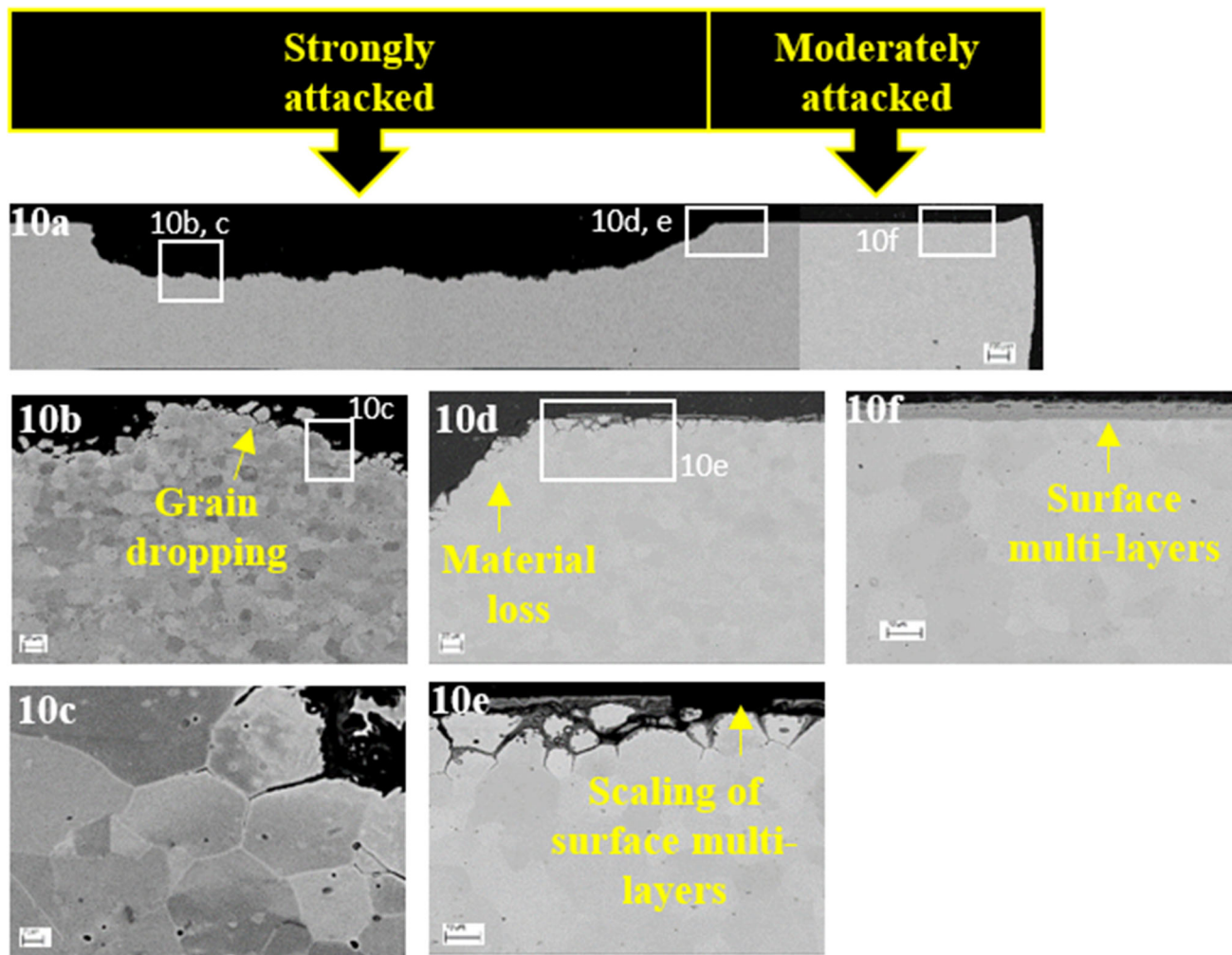
Fig. 10 FE-SEM image of the corroded sample in area B after 100 h experiment (a-f: BS detector, different magnifications and locations). (a) Global view about a corrosion sample showing strongly and moderately attacked areas, and here, three regions of interest were selected for observation under higher magnification (they are marked by the white frame), (b) grain dropping affected by IG corrosion and high corrosion rate, (c) local view of area 10b, showing intergranular attack, (d) global view about a material loss, (e) local view of area 10d about cracked oxide layers and IG attack, (f) global view of moderately attacked area (formation of multioxide layers)

austenite. This is due to the higher diffusion coefficients of interstitial elements C and N in the ferrite. While austenite has a fcc microstructure, ferrite with its bcc microstructure allows higher diffusion rates for these elements. Thus, 1.4016 ferritic stainless steel sample due to the absence of stabilizing elements in its chemical composition resulted in precipitation of $Cr_2N/CrCN$ and consequently in sensitization to intergranular corrosion. The formation of $Cr_2N/CrCN$ will result in a local enrichment of chromium. Consequently, a depletion in chromium in the direct neighborhood of the precipitates will take place. This lower chromium content will result in preferential grain boundary attack. The regular attack associated with some cracking as a result of cyclic heating and cooling has also to be considered.

5. Conclusions

The corroded sample obtained after 100 h of cyclic heating and injection of aqueous urea solution revealed two types of corrosion.

First of all, grade 1.4016 showed similar to 1.4509 uniform corrosion underneath deposits. The mechanism of such a form of corrosion could be explained by high-temperature depassivation of stainless steel due to the excess of the aggressive medium.

Secondly and in contradiction to stabilized material 1.4509, a nitridation layer underneath surface oxides together with chromium carbonitride particles spread through the whole depth of the sample was identified resulting in intergranular attack. The intergranular precipitates appeared to be most detrimental contribution in the current study.

Author Contributions

GM contributed to conceptualization, methodology, validation, data curation, writing—review and editing, and visualization; AG was involved in conceptualization, methodology, validation, investigation, data curation and writing—original draft preparation; FK contributed to methodology, validation, investigation and data

curation; BS was involved in methodology; HW contributed to methodology, validation, data curation, writing—review and editing and visualization; SH was involved in methodology, validation, investigation, data curation, and writing—original draft preparation; SS contributed to methodology; JW was involved in methodology; and SB contributed to methodology, validation, data curation and writing—review and editing.

Funding

Conflict of interest

The authors declare that they have no known competing financial interests or personal relationships that could have appeared to influence the reported in this paper.

Open Access

References

1. L.L. Wei, L.Q. Chen, M.Y. Ma, H.L. Liu, and R.D.K. Misra, Oxidation Behavior of Ferritic Stainless Steels in Simulated Automotive Exhaust Gas Containing 5 vol.% Water Vapor, *Mater. Chem. Phys.*, 2018, **205**, p 508–517. https://doi.org/10.1016/j.matchemphys.2017.11.051

2. X.L. Wang, A.R. Huang, M.X. Li, W. Zhang, C.J. Shang, J.L. Wang, and Z.J. Xie, The significant Roles of Nb and Mo on Enhancement of High Temperature Urea Corrosion Resistance in Ferritic Stainless Steel, *Mater. Lett.*, 2020, **269**, p 127660. https://doi.org/10.1016/j.matlet.2020.127660

3. X. Wang, Q. Lu, W. Zhang, Zh. Xie, and Ch. Shang, Investigation on the Correlation Between Inclusions and High Temperature Urea Corrosion Behavior in Ferritic Stainless Steel, *Metals*, 2021, **11**, p 1823–1832. https://doi.org/10.3390/met11111823

4. Floyd R, Kotrba A, Martin S, Prodin K. Material Corrosion Investigations for Urea SCR Diesel Exhaust Systems. *SAE Int.* (2009)

5. J. Nockert and M. Norell, Corrosion at the Urea Injection in SCR-System during Component Test, *Mater. Corros.*, 2013, **64**, p 34–42. https://doi.org/10.1002/maco.201005983

6. M. Milutinovic, R. Lendjel, S. Balos, D. Zlatanovic, L. Sevsek, and T. Pepelnjak, Characterisation of Geometrical and Physical Properties of a Stainless Steel Denture Framework Manufactured by Single-Point Incremental Forming, *J. Mater. Res. Technol.*, 2021, **10**, p 605–623. https://doi.org/10.1016/j.jmrt.2020.12.014

7. J. Nockert, L. Nyborg, and M. Norell, Corrosion of Stainless Steels in Simulated Diesel Exhaust Environment with Urea, *Mater. Corros.*, 2012, **63**, p 388–395. https://doi.org/10.1002/maco.201005783

8. C. Miraval, S. Saedlou, R. Evrard, P. Santacreu, and J. Leseux, Influence of Selective Catalytic Reduction (SCR) System on Stainless Steel Durability, *REM: Rev Esc. Minas.*, 2013, **66**, p 153–158

9. B. Won-Jin, Y. Kwi-Suba, P. Chan-Jin, R. Han-Jin, and K. Young-Ho, Comparison of Influences of NaCl and CaCl2 on the CORROSION of 11% and 17% Cr Ferritic Stainless Steels during Cyclic Corrosion Test, *Corros. Sci.*, 2010, **52**, p 734–739. https://doi.org/10.1016/j.corsci.2009.10.033

10. J.R. Crum, G.D. Smith, and H.L. Flower, Resistance of Automotive Exhaust Flexible Coupling Alloys to Hot Salt Attack, Stress Corrosion Cracking and High Temperature Embrittlement, *SAE Int. J. Mater. Manuf.*, 1999, **108**, p 403–410

11. H. Zhao, M. Lei, X. Chen, and W. Tang, Facile Route to Metal Nitrides Through Melamine and Metal Oxides, *J. Mat. Chem.*, 2006, **16**, p 4407–4412. https://doi.org/10.1039/b611381h

12. M. Lei, H.Z. Zhao, H. Yang, B. Song, and W.H. Tang, Synthesis of Transition Metal Carbide Nanoparticles through Melamine and Metal Oxides, *J. Eur. Ceram. Soc.*, 2008, **28**, p 1671–1677. https://doi.org/10.1016/j.jeurceramsoc.2007.11.013

13. B. Wei, W. Yang, J. Wang, H. Tan, S. Zhou, and F. Wang, Study on Reduction Mechanism of Fe_2O_3 by NH_3 under SNCR Condition, *Fuel*, 2019, **255**, p 115814. https://doi.org/10.1016/j.fuel.2019.115814

14. S. Saedlou, P. Santacreu, and J. Leseux, Suitable Stainless Steel Selection for Exhaust Line Containing a Selective Catalytic Reduction (SCR) System, *SAE Int.*, 2011 https://doi.org/10.4271/2011-01-1323

15. J. Lu, Z. Yang, B. Zhang, J. Huang, and H. Xu, Corrosion Behavior of Candidate Materials Used for Urea Hydrolysis Equipment in Coal-Fired Selective Catalytic Reduction Units, *J. Mater. Eng. Perform.*, 2018, **27**, p 3290–3296. https://doi.org/10.1007/s11665-017-3001-3

16. M.L. Morgan, Failure Analysis of an 18% Cr Ferritic Stainless Steel in a Simulated Exhaust Condensate Containing Urea, *J. Fail. Anal. Prev.*, 2018, **18**, p 117–120. https://doi.org/10.1007/s11668-018-0387-7

17. A. Galakhova, F. Kadisch, G. Mori, S. Heyder, H. Wieser, B. Sartory, and S. Burger, Corrosion of Stainless Steel by Urea at High Temperature, *Corros. Mater. Degrad.*, 2021, **2**, p 461–473. https://doi.org/10.3390/cmd2030024

18. R.L. Cowan and C.S. Tedmon, Intergranular Corrosion of Iron-Nickel-Chromium Alloys, *Advances in Corrosion Science and Technology*. M.G. Fontana, R.W. Staehle Ed., Springer, New York, 1973